PLOS | NEGLECTED TROPICAL DISEASES

RESEARCH ARTICLE

Seasonal temperature variation influences climate suitability for dengue, chikungunya, and Zika transmission

John H. Huber[1,2], Marissa L. Childs[3], Jamie M. Caldwell[2], Erin A. Mordecai[2]*

1 Department of Applied and Computational Mathematics and Statistics, University of Notre Dame, Notre Dame, Indiana, United States of America, **2** Department of Biology, Stanford University, Stanford, California, United States of America, **3** Emmett Interdisciplinary Program in Environment and Resources, Stanford University, Stanford, California, United States of America

* emordeca@stanford.edu

Check for updates

OPEN ACCESS

Citation: Huber JH, Childs ML, Caldwell JM, Mordecai EA (2018) Seasonal temperature variation influences climate suitability for dengue, chikungunya, and Zika transmission. PLoS Negl Trop Dis 12(5): e0006451. https://doi.org/10.1371/journal.pntd.0006451

Editor: Benjamin Althouse, Institute for Disease Modeling, UNITED STATES

Received: December 6, 2017

Accepted: April 14, 2018

Published: May 10, 2018

Copyright: © 2018 Huber et al. This is an open access article distributed under the terms of the Creative Commons Attribution License, which permits unrestricted use, distribution, and reproduction in any medium, provided the original author and source are credited.

Data Availability Statement: All relevant data are within the paper and its Supporting Information files.

Funding: JHH and EAM were funded by the National Science Foundation (DEB-1518681; www.nsf.gov). EAM was also funded by NSF (DEB-1640780; www.nsf.gov) and the Stanford University Center for Innovation in Global Health (https://globalhealth.stanford.edu/). EAM and JMC were funded by the Stanford University Woods Institute for the Environment, Environmental

Abstract

Dengue, chikungunya, and Zika virus epidemics transmitted by *Aedes aegypti* mosquitoes have recently (re)emerged and spread throughout the Americas, Southeast Asia, the Pacific Islands, and elsewhere. Understanding how environmental conditions affect epidemic dynamics is critical for predicting and responding to the geographic and seasonal spread of disease. Specifically, we lack a mechanistic understanding of how seasonal variation in temperature affects epidemic magnitude and duration. Here, we develop a dynamic disease transmission model for dengue virus and *Aedes aegypti* mosquitoes that integrates mechanistic, empirically parameterized, and independently validated mosquito and virus trait thermal responses under seasonally varying temperatures. We examine the influence of seasonal temperature mean, variation, and temperature at the start of the epidemic on disease dynamics. We find that at both constant and seasonally varying temperatures, warmer temperatures at the start of epidemics promote more rapid epidemics due to faster burnout of the susceptible population. By contrast, intermediate temperatures (24–25˚C) at epidemic onset produced the largest epidemics in both constant and seasonally varying temperature regimes. When seasonal temperature variation was low, 25–35˚C annual average temperatures produced the largest epidemics, but this range shifted to cooler temperatures as seasonal temperature variation increased (analogous to previous results for diurnal temperature variation). Tropical and sub-tropical cities such as Rio de Janeiro, Fortaleza, and Salvador, Brazil; Cali, Cartagena, and Barranquilla, Colombia; Delhi, India; Guangzhou, China; and Manila, Philippines have mean annual temperatures and seasonal temperature ranges that produced the largest epidemics. However, more temperate cities like Shanghai, China had high epidemic suitability because large seasonal variation offset moderate annual average temperatures. By accounting for seasonal variation in temperature, the model provides a baseline for mechanistically understanding environmental suitability for virus transmission by *Aedes aegypti*. Overlaying the impact of human activities and socioeconomic factors onto this mechanistic temperature-dependent framework is critical for understanding likelihood and magnitude of outbreaks.

Ventures Program (https://woods.stanford.edu/research/environmental-venture-projects). MLC acknowledges funding from the Lindsay Family E-IPER Fellowship (https://pangea.stanford.edu/eiper). The funders had no role in study design, data collection and analysis, decision to publish, or preparation of the manuscript.

Competing interests: The authors have declared that no competing interests exist.

Author summary

Mosquito-borne viruses like dengue, Zika, and chikungunya have recently caused large epidemics that are partly driven by temperature. Using a mathematical model built from laboratory experimental data for *Aedes aegypti* mosquitoes and dengue virus, we examine the impact of variation in seasonal temperature regimes on epidemic size and duration. At constant temperatures, both low and high temperatures (20˚C and 35˚C) produce small epidemics, while intermediate temperatures like 25˚C and 30˚C produce much larger epidemics. In seasonally varying temperature environments, epidemics peak more rapidly at higher starting temperatures, while intermediate starting temperatures produce the largest epidemics. Seasonal mean temperatures of 25–35˚C are most suitable for large epidemics when seasonality is low, but in more variable seasonal environments epidemic suitability peaks at lower annual average temperatures. Tropical and sub-tropical cities have the highest temperature suitability for epidemics, but more temperate cities with high seasonal variation also have the potential for very large epidemics.

Introduction

Over the last 30–40 years, arboviral outbreaks have dominated the public health landscape globally [1]. These viruses, most notably dengue (DENV), chikungunya (CHIKV), and Zika (ZIKV), can cause symptoms ranging from rash, arthralgia, and fever to hemorrhagic fever (DENV), long-term arthritis (CHIKV), Guillain-Barré syndrome and microcephaly (ZIKV) [2–4]. DENV, which historically spread worldwide along shipping routes [5], places 3.97 billion individuals at risk worldwide [6] and causes an estimated 390 million cases annually, including 96 million symptomatic cases [7]. CHIKV was introduced into the Americas in December 2013 after an outbreak in St. Martin Island [8]. Since then, autochthonous transmission has been reported in 45 countries [9], and 1.3 billion people worldwide are at risk of contracting CHIKV [10]. More recently, the ZIKV epidemic in the Americas captured global attention after the World Health Organization (WHO) designated it a Public Health Emergency of International Concern in February 2016 in response to its association with neurological disorders. Following the first reported case in Brazil in May 2015, ZIKV has spread to 48 countries and territories where it is transmitted autochthonously [11]. Because DENV, CHIKV, and ZIKV are mostly transmitted by *Aedes aegypti* mosquitoes, they may have similar geographic distributions and risk factors.

Informed public health decisions to limit the spread and magnitude of these arboviral epidemics depend on a robust understanding of transmission dynamics. One mechanistic modeling framework, the Susceptible–Infected–Recovered (SIR) model, has been implemented successfully to model the dynamics of outbreaks of influenza, measles, and vector-borne diseases such as CHIKV and ZIKV [12–14]. This approach tracks virus population dynamics by compartmentalizing individuals by their state in an epidemic (i.e., Susceptible (S), Infected (I), Recovered (R)). This framework can be extended to include additional compartments, such as a latency stage, or to incorporate the dynamics of the mosquito population for vector transmission.

Arbovirus dynamics are strikingly seasonal and geographically restricted to relatively warm climates [6,7]. This arises because several life history traits of the mosquitoes that transmit DENV, CHIKV, and ZIKV are strongly influenced by temperature and seasonality [15–22]. For simplicity, many existing models assume static life history traits [14], and those that address seasonal forcing tend to incorporate sinusoidal variation as a single transmission

parameter, β [23]. Treating seasonal temperature variation as a sinusoidal forcing function on the transmission parameter implies a monotonic relationship between temperature and transmission, such that transmission is maximized at high temperatures and decreases at low temperatures. However, decades of experimental work have demonstrated strongly nonlinear (often unimodal) relationships between mosquito and pathogen traits and temperature that are not well captured in a single sinusoidal forcing function [24]. Efforts by Yang et al. [25,26] addressed the need to include seasonal variation by adopting an SEI-SEIR compartmental framework with time-varying entomological parameters and fitting the model to DENV incidence data in Campinas, Brazil. Other previous work has integrated the effects of temperature on mosquito and parasite traits into temperature-dependent transmission models for DENV, CHIKV, and/or ZIKV, and revealing a strong, nonlinear influence of temperature with peak transmission between 29–35˚C [27–34]. However, we do not yet have a mechanistic estimate for the relationship between seasonal temperature regimes and transmission potential, incorporating the full suite of transmission-relevant, nonlinear thermal responses of mosquito and parasite traits.

Here, we expand on previous work with three main advances: (1) we incorporate the full suite of empirically-derived, unimodal thermal responses for all known transmission-relevant mosquito and parasite traits; (2) we examine the influence of seasonal temperature mean and variation (in contrast to constant temperatures or daily temperature variation); and (3) we use a dynamic transmission framework to explore the impact of different seasonal temperature regimes on the epidemiologically-relevant outcomes of epidemic size, duration, and peak incidence (in contrast to R_0, or vectorial capacity, which are difficult to measure directly). To do so, we incorporate previously estimated and independently validated thermal response functions for all vector and parasite traits [24] into a dynamic SEI-SEIR model [25,26]. We explore field-relevant temperature regimes by simulating epidemics across temperature means (10–38˚C) and seasonal ranges (0–17˚C) from across the predicted suitable range for transmission. Specifically, we use the model to ask: (1) How does final epidemic size vary across constant temperatures? (2) Under seasonally varying temperatures, how does the temperature at the start of the epidemic affect the final epidemic size and duration? (3) How do temperature mean and seasonal range interact to determine epidemic size? (4) Which geographic locations have high epidemic suitability based on climate?

Methods

Model

Model framework. We adopted an SEI-SEIR compartmental modeling framework to simulate arboviral transmission by the *Aedes aegypti* vector (Fig 1). We introduced temperature-dependence into the model by using fitted thermal response curves for the mosquito life history traits provided by Mordecai et al. [24]. The full model is:

$$\frac{dS_V}{dt} = EFD(T) * pEA(T) * MDR(T) * \mu(T)^{-1} * N_V * \left(1 - \frac{N_V}{K(T)}\right) - \left(a(T) * pMI(T) * \frac{I_H}{N_H} + \mu(T)\right) * S_V, \quad (1)$$

$$\frac{dE_V}{dt} = a(T) * pMI(T) * \frac{I_H}{N_H} * S_V - (PDR(T) + \mu(T)) * E_V, \quad (2)$$

$$\frac{dI_V}{dt} = PDR(T) * E_V - \mu(T) * I_V, \quad (3)$$

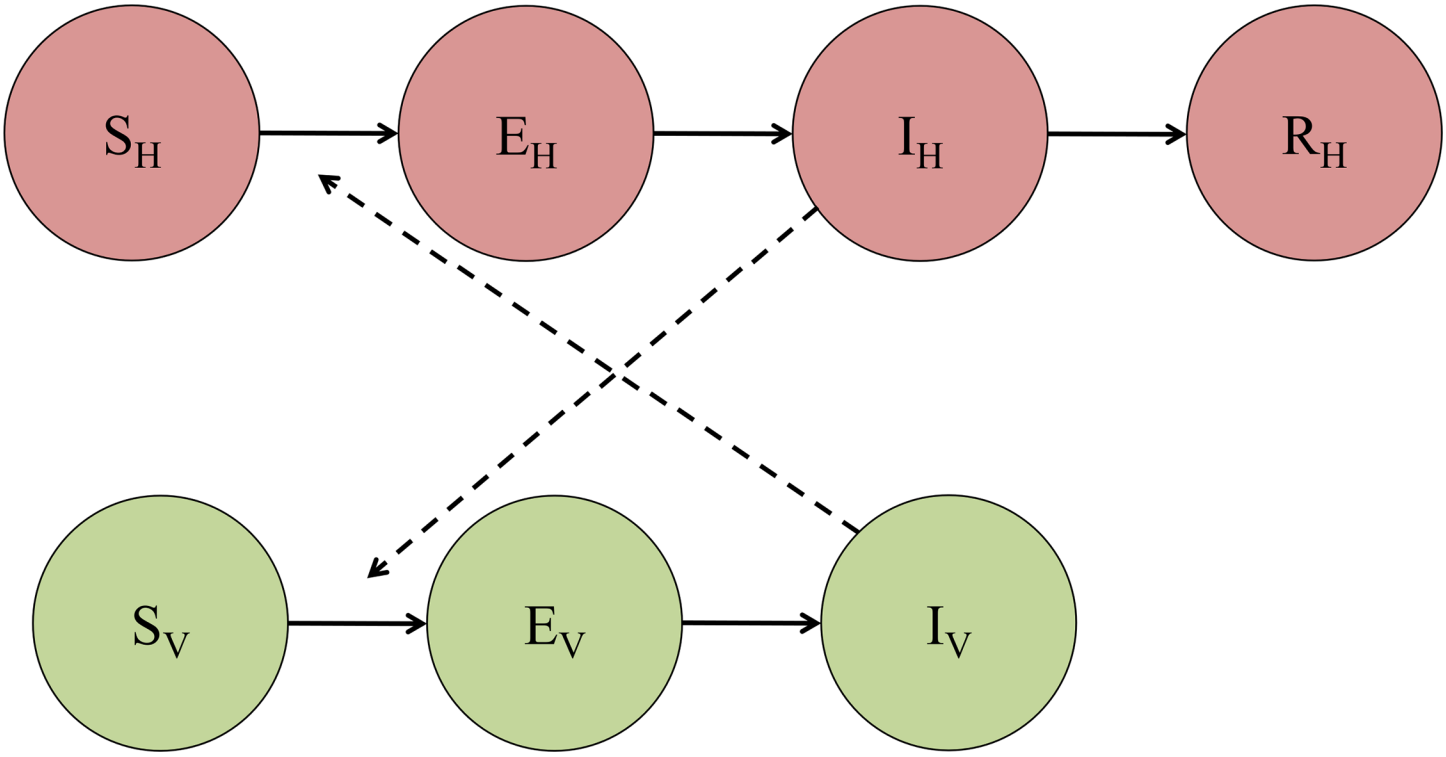

Fig 1. Compartmental model of transmission. S_H, E_H, I_H, and R_H represent the susceptible, exposed (or latent), infectious, and recovered segments of the human population, respectively. Likewise, S_V, E_V, and I_V represent the susceptible, exposed (or latent), and infectious segments of the mosquito population. Solid arrows signify the directionality of transition from one compartment to the next, and dashed arrows indicate the directionality of transmission.

https://doi.org/10.1371/journal.pntd.0006451.g001

$$\frac{dS_H}{dt} = -a(T) * b(T) * \frac{I_V}{N_H} * S_H, \tag{4}$$

$$\frac{dE_H}{dt} = a(T) * b(T) * \frac{I_V}{N_H} * S_H - \delta * E_H, \tag{5}$$

$$\frac{dI_H}{dt} = \delta * E_H - \eta * I_H, \tag{6}$$

$$\frac{dR_H}{dt} = \eta * I_H, \tag{7}$$

The SEI portion of the model describes the vector population, where S_V represents the number of susceptible mosquitoes, E_V is the number of mosquitoes in the latency stage, and I_V is the number of infectious mosquitoes. We assumed that *Aedes aegypti* mosquitoes remain infectious until they die. In Eqs 1–3, *(T)* indicates temperature-dependent functions, *EFD(T)* is the number of eggs laid per female per day, *pEA(T)* is the probability of mosquito egg-to-adult survival, *MDR(T)* is the mosquito egg-to-adult development rate, N_V is the total mosquito population at time t (i.e., $S_v + E_v + I_v$), *K(T)* is the carrying capacity for the mosquito population, *a(T)* is the per mosquito biting rate, *pMI(T)* is the probability of mosquito infection per bite on

Table 1. Fitted thermal responses for *Aedes aegypti* life history traits. Traits were fit to a Brière $[cT(T - T_0)(T_m - T)^{\frac{1}{2}}]$ or a quadratic $[c(T - T_m)(T - T_0)]$ function where T represents temperature. T_0 and T_m are the critical thermal minimum and maximum, respectively, and c is the rate constant. Thermal responses were fit by [24].

Trait	Definition	Function	Fitted Parameters		
a	Biting rate (day^{-1})	Brière	c = 2.02e-04	T_{min} = 13.35	T_{max} = 40.08
EFD	Eggs laid per female per day	Brière	c = 8.56e-03	T_{min} = 14.58	T_{max} = 34.61
pEA	Probability of mosquito egg-to-adult survival	Quadratic	c = -5.99e-03	T_{min} = 13.56	T_{max} = 38.29
MDR	Mosquito egg-to-adult development rate (day^{-1})	Brière	c = 7.86e-05	T_{min} = 11.36	T_{max} = 39.17
lf	Adult mosquito lifespan (days)	Quadratic	c = -1.48e-01	T_{min} = 9.16	T_{max} = 37.73
b	Probability of mosquito infectiousness	Brière	c = 8.49e-04	T_{min} = 17.05	T_{max} = 35.83
pMI	Probability of mosquito infection	Brière	c = 4.91e-04	T_{min} = 12.22	T_{max} = 37.46
PDR	Virus extrinsic incubation rate (day^{-1})	Brière	c = 6.65e-05	T_{min} = 10.68	T_{max} = 45.90

https://doi.org/10.1371/journal.pntd.0006451.t001

an infectious host, $\mu(T)$ is the adult mosquito mortality rate, and $PDR(T)$ is the parasite development rate. Each life history and pathogen transmission trait of the *Aedes aegypti* mosquito is a unimodal, temperature-dependent function fit from experimental laboratory data in previous work [15–22,24] (Table 1; Appendix; "Functional Forms of Life History Traits").

The SEIR portion of the model describes the human population, where S_H represents the number of susceptible individuals, E_H the number of latent (or exposed) individuals, I_H the number of infectious individuals, and R_H the number of recovered individuals. We assumed a static population size, N_H, that was neither subject to births nor deaths because the human lifespan far exceeds the duration of an epidemic. Further, we binned asymptomatic and symptomatic individuals into a single infectious class since asymptomatic infections have been shown to transmit DENV [35] and exhibit similar viremic profiles as symptomatic patients in CHIKV [36]. Based on previous arboviral outbreaks [37,38], we assumed that an infection conferred long-term immunity to an individual. Thus, a previously infectious individual entering the recovered class is protected from subsequent re-infection for the remainder of the epidemic. In the case of dengue, where there are four unique serotypes, we consider single-season epidemics of a single serotype. In Eqs 4–7, $b(T)$ is the probability of human infection per bite by an infectious mosquito (Table 1), δ^{-1} is the intrinsic incubation period, and η^{-1} is the human infectivity period. Since human components of the transmission cycle are not seasonal, we used constants of 5.9 days for the intrinsic incubation period, $1/\delta$, and 5.0 days for the infectious period, $1/\eta$ [14]. All temperature-independent parameter values are given in Table 2.

Since the lifespan of an adult mosquito is short relative to the timespan of an epidemic, we allowed mosquito birth and death rates to drive population dynamics. Additionally, the birth rate of susceptible mosquitoes was regulated by a temperature-dependent carrying capacity, K (Eq 8), which we modeled as a modified Arrhenius equation that is a unimodal function of

Table 2. Values of temperature-independent parameters used in the model, and their sources.

Parameter	Definition	Value	Source
δ^{-1}	Intrinsic incubation period (days)	5.9	[14]
η^{-1}	Human infectivity period (days)	5.0	[14]
I_0^H / N	Proportion of initially infectious humans	0.0001	
I_0^V / M	Proportion of initially infectious mosquitoes	0.015	[14]
M / N	Ratio of mosquitoes-to-humans at 29˚C	2.0	[39]

https://doi.org/10.1371/journal.pntd.0006451.t002

temperature [40]:

$$K(T) = \frac{EFD(T_0) * pEA(T_0) * MDR(T_0) * \mu(T_0)^{-1} - \mu(T_0)}{EFD(T_0) * pEA(T_0) * MDR(T_0) * \mu(T_0)^{-1}} * N_m * e^{\frac{-E_A*(T-T_0)^2}{\kappa_B*(T+273)*(T_0+273)}}, \quad (8)$$

Here, T_0 is defined as the reference temperature (i.e., the temperature at which the carrying capacity is greatest) in Celsius, N_m is the maximum carrying capacity, and κ_B is Boltzmann constant (8.617 x 10^{-5} eV/K). *EFD* is the number of eggs laid per female per day, *pEA* is the probability of egg-to-adult mosquito survival, *MDR* is the mosquito egg-to-adult development rate, and μ is the adult mosquito mortality rate. We calculated these values for the reference temperature. E_A is the activation energy, which we set to 0.5 and represents the temperature dependence of the carrying capacity, a conservative estimate as we lacked sufficient data on estimates of the carrying capacity of *Aedes aegypti* and its underlying temperature dependence. To convert from Celsius to Kelvin, we incremented the temperature T and the reference temperature T_0 by 273. Eq (8) was adopted from [40] and modified to allow the distribution to be unimodal. We set the reference temperature, T_0, to 29˚C, which is consistent with optimal temperatures for *Aedes aegypti* transmission [24,29].

We included a temperature-dependent carrying capacity in the model to constrain the growth of the mosquito population. As described in the Appendix, all simulations begin with the mosquito population at its (temperature-dependent) carrying capacity. As the temperature changes seasonally, the mosquito population does not necessarily remain at carrying capacity if one or more of the life history traits that determine the production of new mosquitoes in Eq (1)—*EFD*, *pEA*, and *MDR*—is equal to zero. This occurs below 14.58˚C (the highest T_{min} of *EFD*, *pEA*, and *MDR*) or above 34.61˚C (the lowest T_{max} of *EFD*, *pEA*, and *MDR*).

It should be noted that the transmission parameters are only related to the current temperature at each time point in the simulation. Time lags for each life history trait were not explicitly built into the model.

Seasonal forcing. To address seasonality in the model, we allowed temperature to vary over time. We modeled temperature as a sinusoidal curve with a period of 365 days of the form:

$$T(t) = \frac{T_{max} - T_{min}}{2} * \sin\left(\frac{2\pi}{365}t\right) + T_{mean}, \quad (9)$$

Here, T_{max}, T_{mean}, and T_{min} represent the average monthly maximum, mean, and minimum temperatures across a calendar year, respectively, and t is measured in days. By modeling temperature as a function of time, we allowed the life history traits of the *Aedes aegypti* vector to vary across time for the duration of the epidemic. In the absence of a specific focal location we modeled seasonal temperature as a sinusoidal function for simplicity.

Data

Life history traits. To incorporate seasonal forcing into the compartmental modeling framework, we used fitted mechanistic thermal response curves [24]. Mordecai et al. [24] examined published data on thermal responses for life history traits of the *Aedes aegypti* vector and DENV and adopted a Bayesian approach for fitting quadratic ($Q(T)$; Eq 10) or Brière ($B(T)$; Eq 11) curves (see Appendix for details).

$$Q(T) = c * (T - T_{min}) * (T - T_{max}), \quad (10)$$

$$B(T) = c * T * (T - T_{min}) * \sqrt{T_{max} - T}, \quad (11)$$

Table 3. Temperature regimes for major cities during the 2016 calendar year. Monthly mean temperatures during 2016 were extracted from Weather Underground.

City	Annual Mean Temperature (˚C)	Annual Temperature Amplitude (˚C)
Buenos Aires, Argentina	16.5	8.0
Sao Paulo, Brazil	20.6	5.0
Rio de Janeiro, Brazil	24.3	4.0
Salvador, Brazil	26.3	2.0
Fortaleza, Brazil	27.8	0.50
Belo Horizonte, Brazil	21.9	3.0
Recife, Brazil	27.2	1.5
Shanghai, China	17.6	12.5
Beijing, China	12.8	16
Guangzhou, China	22.9	8.0
Bogotá, Colombia	14.7	1.0
Medellin, Colombia	17.9	1.0
Cali, Colombia	25.1	1.5
Barranquilla, Colombia	28.8	1.0
Cartagena, Colombia	28.6	1.0
Delhi, India	26.3	9.5
Tokyo, Japan	17.0	10.5
Kobe, Japan	17.4	11
Manila, Philippines	29.0	1.5
New York, USA	13.8	12

https://doi.org/10.1371/journal.pntd.0006451.t003

Here, c is a rate constant, T_{min} is the critical temperature minimum, and T_{max} is the critical temperature maximum (Table 1). Following Mordecai et al. [24], we assumed values above the critical thermal maxima and below the minima were equal to zero.

Mordecai et al. [24] fit the thermal response for adult mosquito lifespan (Table 1), the inverse of the adult mosquito mortality rate (μ, in days^{-1}), used in our model. We set the mortality rate at temperatures outside the critical thermal minimum and maximum to 24 days^{-1} (i.e., mosquitoes survive for one hour at temperatures outside of the T_{min} to T_{max} range).

Historical weather data. To identify areas of epidemic suitability across the globe, we extracted monthly mean temperatures for 2016 from Weather Underground (wunderground.com) for twenty different cities (Table 3). For each city, we calculated the mean, minimum, and maximum from the average monthly mean temperatures, to estimate temperature seasonality. This provided a range of the average monthly temperature over the span of a calendar year. We chose this time period because it provided the most recent full calendar year to demonstrate seasonal variation in temperature.

Variability in epidemic dynamics with constant temperature

We first examined how epidemic dynamics varied across different constant temperatures. Here, we did not introduce seasonal forcing into the model but rather assumed static life history traits for *Aedes aegypti* for the simulation period. We simulated the model under default starting conditions (see Appendix) at four different constant temperatures: 20˚C, 25˚C, 30˚C, and 35˚C. These temperatures were chosen to span the range of temperatures at which arbovirus transmission is likely to be possible [24].

Variability in epidemic dynamics with starting temperature

Using the model that included seasonal variation in temperature, we examined how the dynamics of an epidemic varied due to the temperature at which the epidemic began, under two temperature regimes. First, we set T_{max} = 40.0˚C, T_{mean} = 25.0˚C, and T_{min} = 10.0˚C in the time-varying seasonal temperature model under default parameters (see Appendix) and varied the temperature at the start of the epidemic from 10.0˚C to 40.0˚C in increments of 0.1˚C. We examined the response of final epidemic size, epidemic length, and maximum instantaneous number of infected individuals. We then repeated this process for a regime with a lower magnitude of seasonal temperature variation: T_{max} = 30.0˚C, T_{mean} = 25.0˚C, and T_{min} = 20.0˚C. By comparing these temperature regimes, we can examine how epidemics respond to starting temperatures that are outside the range of plausible temperatures of arbovirus transmission (regime 1) versus restricted to the plausible temperatures for transmission (regime 2) [24].

Seasonal variability of final epidemic size

Using the compartmental modeling framework with the default starting conditions, we examined the variation in final epidemic size as a result of seasonal forcing. To do so, we simulated over a wide range of temperature mean and seasonal variance regimes. The mean annual temperature varied from 10.0˚C to 38.0˚C in increments of 0.1˚C, while the seasonal variation about the mean (i.e., $\frac{T_{max}-T_{min}}{2}$) ranged from 0.0˚C to 17.0˚C in increments of 0.1˚C. Many of these temperature regimes are unlikely to be observed empirically. However, the simulated temperature regimes spanned the full range of feasible temperature conditions. We recorded the final epidemic size, measured as the number of individuals in the recovered compartment at the end of the simulation, for each unique combination of mean annual temperature and seasonal variation. In addition, we examined the effect of epidemic starting temperature on final epidemic size across the same seasonal temperature regimes. We ran the model under default starting conditions, but allowed the starting temperature to equal T_{min}, T_{mean}, or T_{max}.

To observe the interaction of population immunity with the seasonal temperature regime, we simulated the model assuming that 0, 20, 40, 60, or 80% of the population was initially immune. Each simulation began with the introduction of the infected individual occurring at the mean seasonal temperature.

We then compared simulated climate regimes with actual climates in major cities, to measure relative epidemic suitability of the following cities: São Paulo, Brazil; Rio de Janeiro, Brazil; Salvador, Brazil; Fortaleza, Brazil; Belo Horizonte, Brazil; Recife, Brazil; Bogotá, Colombia; Medellín, Colombia; Cali, Colombia; Barranquilla, Colombia; Cartagena, Colombia; Tokyo, Japan; Delhi, India; Manila, Philippines; Shanghai, China; Beijing, China; New York City, USA; Guangzhou, China; Kobe, Japan; and Buenos Aires, Argentina, given 0, 20, 40, 60, and 80% population immunity. These cities were chosen because they represent some of the most populous urban areas across South America and throughout the world.

Model sensitivity and uncertainty analysis

To characterize uncertainty in the model, we sampled 50 joint posterior estimates for c, T_{min}, and T_{max} for each life history trait provided by Mordecai et al. [24]. We examined the variability in epidemic dynamics with starting temperatures under each parameterization and report the 95% credible interval for the epidemiological indices. We similarly characterize uncertainty in our estimates of the final epidemic size as a function of the seasonal temperature regime by simulating under each parameterization and reporting the 95% credible interval.

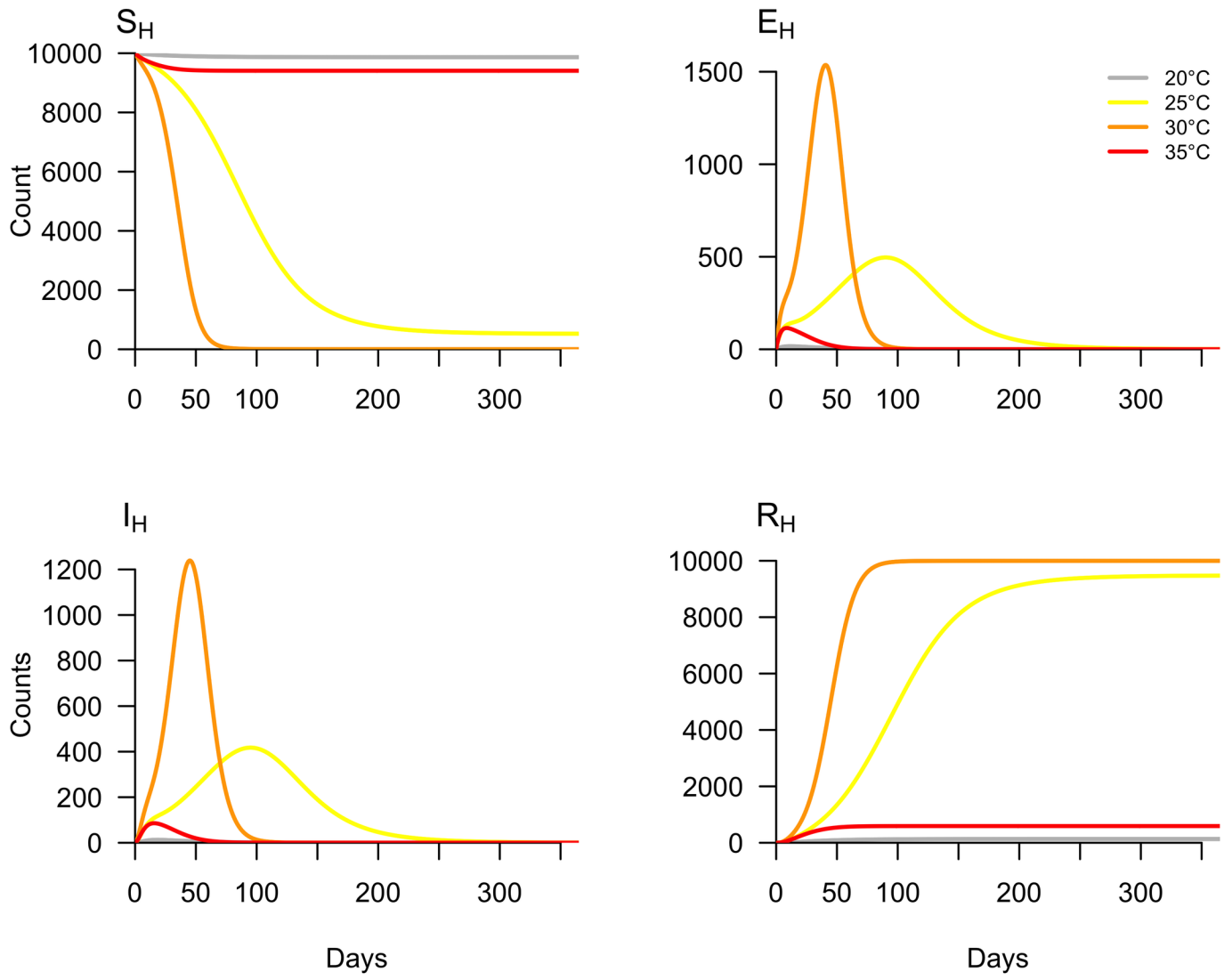

Fig 2. Variation in epidemic dynamics by temperature. The model was simulated under default parameters at four constant temperatures: 20˚C, 25˚C, 30˚C, and 35˚C.

https://doi.org/10.1371/journal.pntd.0006451.g002

Results

Variability in epidemic dynamics with constant temperature

Holding temperature constant, we examined variability in epidemic dynamics across four temperatures: 20˚C, 25˚C, 30˚C, and 35˚C. As temperature increased from 20˚C to 30˚C, the number of susceptible individuals depleted more rapidly (Fig 2, S_H). At 20˚C and 35˚C, the epidemics were small (1.33% and 5.92% of the population infected, respectively) and burned out rapidly. Although simulations run at 25˚C and 30˚C produced final epidemic sizes of 94.73% and 99.98% of the population infected, respectively (Fig 2, R_H), the epidemic peaked much faster at 30˚C.

Variability in epidemic dynamics with starting temperature

Next, we examined variability in epidemic dynamics due to the temperature at which the epidemic began, given two seasonal temperature regimes (25˚C mean and a seasonal range of

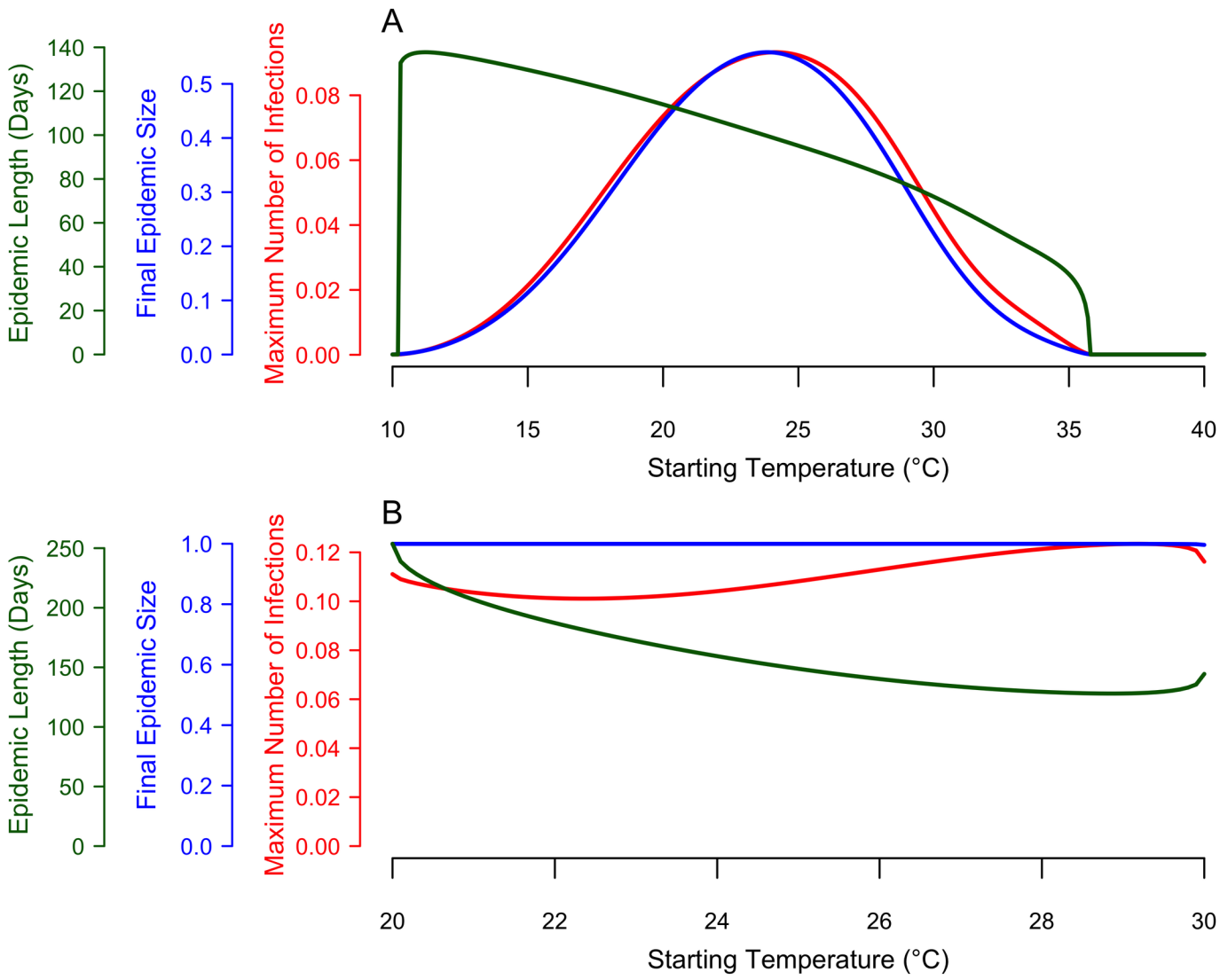

Fig 3. Epidemiological indices as a function of starting temperature, within a given seasonal temperature regime. The red curve represents the maximum number of humans in the infected class (I_H) at any given point during the simulation. The blue curve represents the final (or cumulative) epidemic size (R_H at the final time step). The green curve represents the length of the epidemic (i.e., the point at which the number of infected individuals was below one). Here, simulations were run with the temperature conditions: T_{min} = 10˚C, T_{mean} = 25˚C, and T_{max} = 40˚C (A) and T_{min} = 20˚C, T_{mean} = 25˚C, and T_{max} = 30˚C (B).

https://doi.org/10.1371/journal.pntd.0006451.g003

10˚C to 40˚C or 20˚C to 30˚C, respectively). Given that an epidemic occurred, epidemic length monotonically decreased as a function of starting temperature for the first temperature regime (Fig 3A): warmer temperatures at the start of the epidemic produced shorter epidemics, and vice versa. In the second temperature regime, epidemic length monotonically decreased as a function of starting temperature until ~29˚C. When temperature varied from 10˚C to 40˚C, the longest epidemic simulated was 137.8 days and occurred at starting temperatures of 11.2˚C, and the shortest epidemic lasted 16.82 days and occurred when the temperature at the epidemic start was 35.7˚C. When the temperature was 35.8˚C or higher or 10.2˚C or lower, no epidemic occurred. When temperature was constrained between 20˚C and 30˚C, the longest epidemic simulated was 253.64 days at a starting temperature of 20˚C, and the shortest epidemic lasted 136.1 days at a starting temperature of 28.9˚C.

In contrast to epidemic length, the response of final epidemic size and maximum number of infected individuals to the temperature at epidemic onset depended on the amount of seasonal temperature variation. When temperature varied widely, from 10˚C to 40˚C, both final epidemic size and the maximum number of infected individuals responded unimodally to starting temperature, with peaks at 23.9˚C and 24.1˚C, respectively (Fig 3A). By contrast, when temperature varied more narrowly from 20˚C to 30˚C, the final epidemic size and the maximum number of infected individuals were insensitive to starting temperature (Fig 3B). Taken together, these results show that epidemics introduced at different times within identical seasonal temperature regimes can produce very similar final epidemic sizes and maximum infection rates, provided that the temperature range is sufficiently constrained. If temperature variation is large, dramatically different final epidemic sizes and maximum infection rates may result.

Seasonal variability of final epidemic size

To address how mean temperature and seasonal variance combined to influence the final epidemic size, we simulated over a wide range of temperature regimes that accounted for variation in the mean and temperature range over a calendar year. We calculated relative epidemic suitability, defined as the final epidemic size as a proportion of the human population, for twenty major cities worldwide (Table 4).

In a low-variation thermal environment, a band of mean temperatures between approximately 25˚C and 35˚C supports the highest epidemic suitability (Fig 4). As the seasonal temperature range increases, lower mean temperatures are capable of supporting large epidemics.

Table 4. Estimates of epidemic suitability for major cities. Epidemic suitability was calculated as the proportion of the population that became infected in simulations run with 0, 20, 40, 60, or 80% initial population immunity. Temperature at simulation onset was set to the mean of the temperature regime. Each city was simulated with its respective temperature regime from the 2016 calendar year.

	Epidemic Suitability				
City	**0% Immunity**	**20% Immunity**	**40% Immunity**	**60% Immunity**	**80% Immunity**
Buenos Aires, Argentina	0.03656	0.02169	0.01203	0.005975	0.002295
Sao Paulo, Brazil	0.6056	0.3386	0.1518	0.05351	0.01385
Rio de Janeiro, Brazil	0.9984	0.7962	0.5891	0.3618	0.09862
Salvador, Brazil	0.9990	0.7976	0.5937	0.3804	0.1335
Fortaleza, Brazil	0.9993	0.7982	0.5953	0.3861	0.1535
Belo Horizonte, Brazil	0.5909	0.3344	0.1544	0.05771	0.01633
Recife, Brazil	0.9994	0.7985	0.5959	0.3871	0.1517
Shanghai, China	0.9966	0.7878	0.5507	0.2484	0.03456
Beijing, China	0.5268	0.2526	0.09058	0.02298	0.003587
Guangzhou, China	0.9996	0.7989	0.5965	0.3848	0.1254
Bogotá, Colombia	0.0001000	0.0001000	0.0001000	0.0001000	0.0001000
Medellin, Colombia	0.002544	0.002048	0.001556	0.001068	0.0005820
Cali, Colombia	0.9909	0.7822	0.5617	0.3122	0.07217
Barranquilla, Colombia	0.9997	0.7993	0.5979	0.3928	0.1703
Cartagena, Colombia	0.9997	0.7993	0.5978	0.3923	0.1688
Delhi, India	0.9537	0.7215	0.4759	0.2388	0.06803
Tokyo, Japan	0.7269	0.4149	0.1758	0.05159	0.009489
Kobe, Japan	0.9435	0.6669	0.3522	0.1090	0.01632
Manila, Philippines	0.9998	0.7994	0.5981	0.3933	0.1720
New York, USA	0.04088	0.02159	0.01041	0.004390	0.001425

https://doi.org/10.1371/journal.pntd.0006451.t004

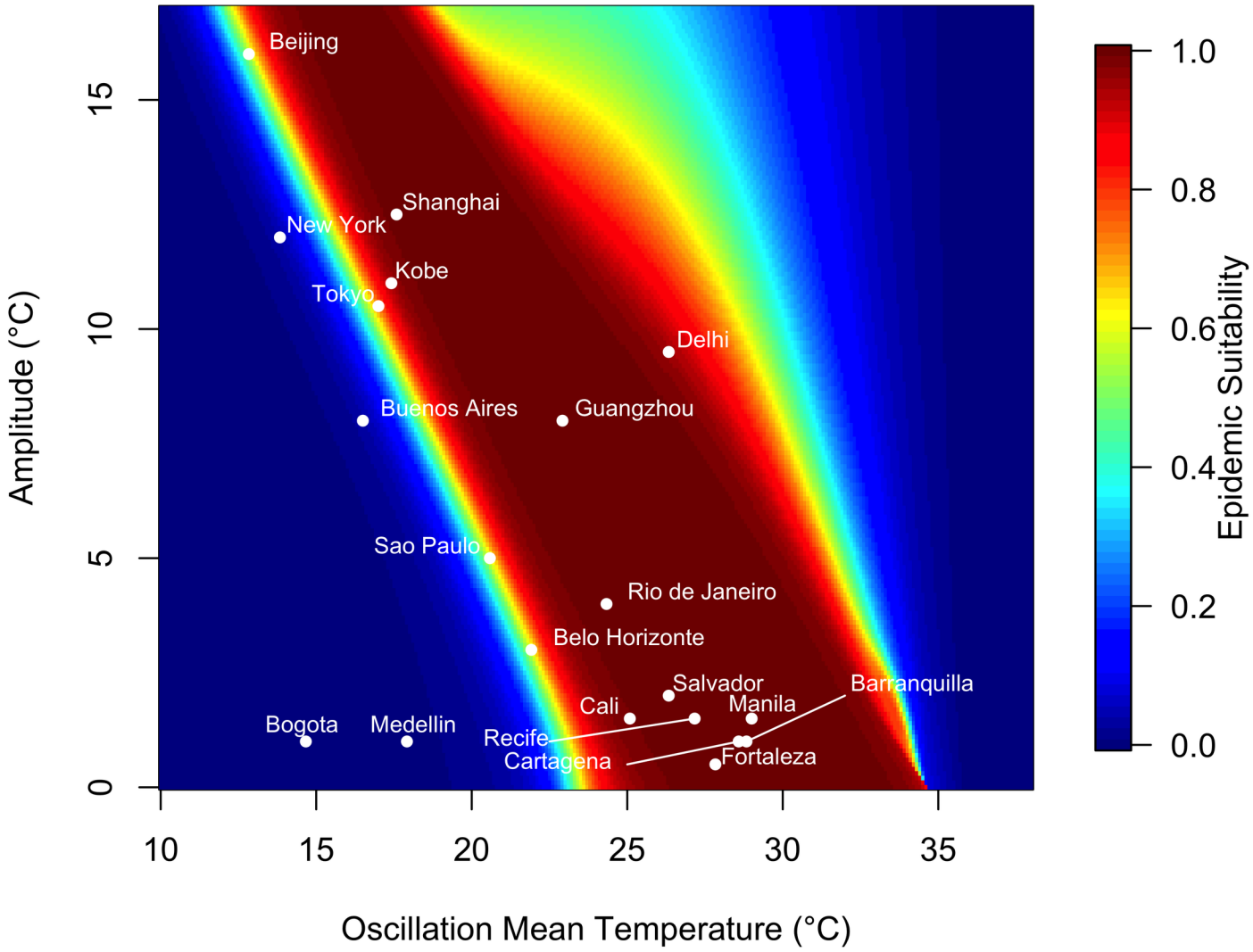

Fig 4. Variation in epidemic suitability across different seasonal temperature regimes. The heat map shows the epidemic suitability (represented as the proportion of the total human population infected during an epidemic) as a function of mean annual temperature and temperature range. Here, temperature range is defined as the seasonal variation about the annual mean temperature. Twenty large, globally important cities are plotted to illustrate their epidemic suitability.

https://doi.org/10.1371/journal.pntd.0006451.g004

However, outside this narrow band of temperature regimes, epidemic suitability rapidly diminishes, and most temperature regimes did not produce epidemics.

Of the focal 20 major cities, those with high mean temperature and small average temperature variation exhibited the highest epidemic suitability. For instance, Manila, Philippines, which has a monthly mean temperature of 29˚C and average seasonal amplitude in mean temperature of 1.50˚C, had an epidemic suitability of 0.9998. Cartagena and Barranquilla, Colombia had epidemic suitability of 0.9997. On the other hand, areas with low average temperature and greater temperature variation, such as Beijing and New York, exhibited lower—but still non-zero—epidemic suitabilities of 0.5268 and 0.04088 respectively. Notably, Guangzhou and Shanghai, China have high epidemic suitability (0.9996 and 0.9966, respectively) despite moderate mean temperatures (22.9 and 17.6˚C, respectively) due to high seasonal variation in temperature. By contrast, high seasonal variation reduced suitability to 0.9537 in Delhi, India, which has a high mean temperature of 26.3˚C (Fig 4).

Table 5. Estimates of epidemic suitability for major cities under different starting temperatures. Epidemic suitability was calculated as the proportion of the population that became infected in simulations that began at the minimum, mean, or maximum temperature of the seasonal temperature regime. Each city was simulated with its respective temperature regime from the 2016 calendar year with 0% population immunity.

	Epidemic Suitability		
City	**Minimum Starting Temperature**	**Mean Starting Temperature**	**Maximum Starting Temperature**
Buenos Aires, Argentina	0.0001000	0.03656	0.1166
Sao Paulo, Brazil	0.02026	0.6056	0.3480
Rio de Janeiro, Brazil	0.9978	0.9984	0.9760
Salvador, Brazil	0.9965	0.9990	0.9963
Fortaleza, Brazil	0.9986	0.9993	0.9990
Belo Horizonte, Brazil	0.09404	0.5909	0.3273
Recife, Brazil	0.9973	0.9994	0.9987
Shanghai, China	0.0001000	0.9966	0.8905
Beijing, China	0.0001000	0.5268	0.5792
Guangzhou, China	0.9983	0.9996	0.9912
Bogotá, Colombia	0.0001000	0.0001000	0.0001000
Medellin, Colombia	0.0002177	0.002544	0.004472
Cali, Colombia	0.9858	0.9909	0.9623
Barranquilla, Colombia	0.9994	0.9997	0.9997
Cartagena, Colombia	0.9993	0.9997	0.9997
Delhi, India	0.5615	0.9537	0.6954
Tokyo, Japan	0.0001000	0.7269	0.5121
Kobe, Japan	0.0001000	0.9435	0.6890
Manila, Philippines	0.9994	0.9998	0.9998
New York, USA	0.0001000	0.04088	0.1863

https://doi.org/10.1371/journal.pntd.0006451.t005

The relationship between epidemic suitability and seasonal temperature regime was consistent across varying levels of population immunity. Locations with high mean temperatures and small average temperature variation had higher epidemic suitability, regardless of the level of population immunity (S8–S10 Figs). However, as the level of immunity increased from 20% to 80%, the epidemic suitability at given seasonal temperature regime decreased (Table 4).

Epidemic suitability also varied by starting temperature, depending on the seasonal temperature regime. The epidemic suitability of cities with high mean temperature and small average temperature variation—such as Manila, Philippines and Cartagena and Barranquilla, Colombia—did not depend on starting temperature (Table 5). However, areas with low to moderate mean temperature and large average temperature variation (e.g., Kobe, Japan and Shanghai, China) exhibited low epidemic suitability (both 0.0001000) at the minimum starting temperature and moderate-to-high epidemic suitability at the maximum starting temperature (0.6890 and 0.8905, respectively) (Fig 5). The opposite occurred in regimes with high mean temperature and large temperature variation, though these temperature regimes are rarer.

Estimated epidemic suitability is close to one in the most suitable temperature regimes because we assumed that: (i) the population was fully susceptible at the start of the epidemic; (ii) mixing was homogeneous among humans and mosquitoes; (iii) all cases of infection are included regardless of whether or not they are symptomatic; and (iv) no other environmental or social drivers are limiting transmission. As a result, the epidemic suitability metric should be considered an upper bound on the proportion of the population that could become infected based on temperature alone.

Model sensitivity and uncertainty analysis

Final epidemic size was not sensitive to life history trait parameterization (S8–S10 Figs), using samples from the posterior distribution of thermal response fits for each temperature-dependent trait.

There was uncertainty in the specific numerical values of the epidemiological indices across starting temperatures (S1 Fig). However, the overall functional response of the final epidemic size, maximum number of infected individuals, and the epidemic length to starting temperature was consistent across the samples from the joint posterior distribution.

Discussion

Recent outbreaks of DENV, CHIKV, and ZIKV in Latin America and across the globe have captured the attention of the public health community and underscore the importance of

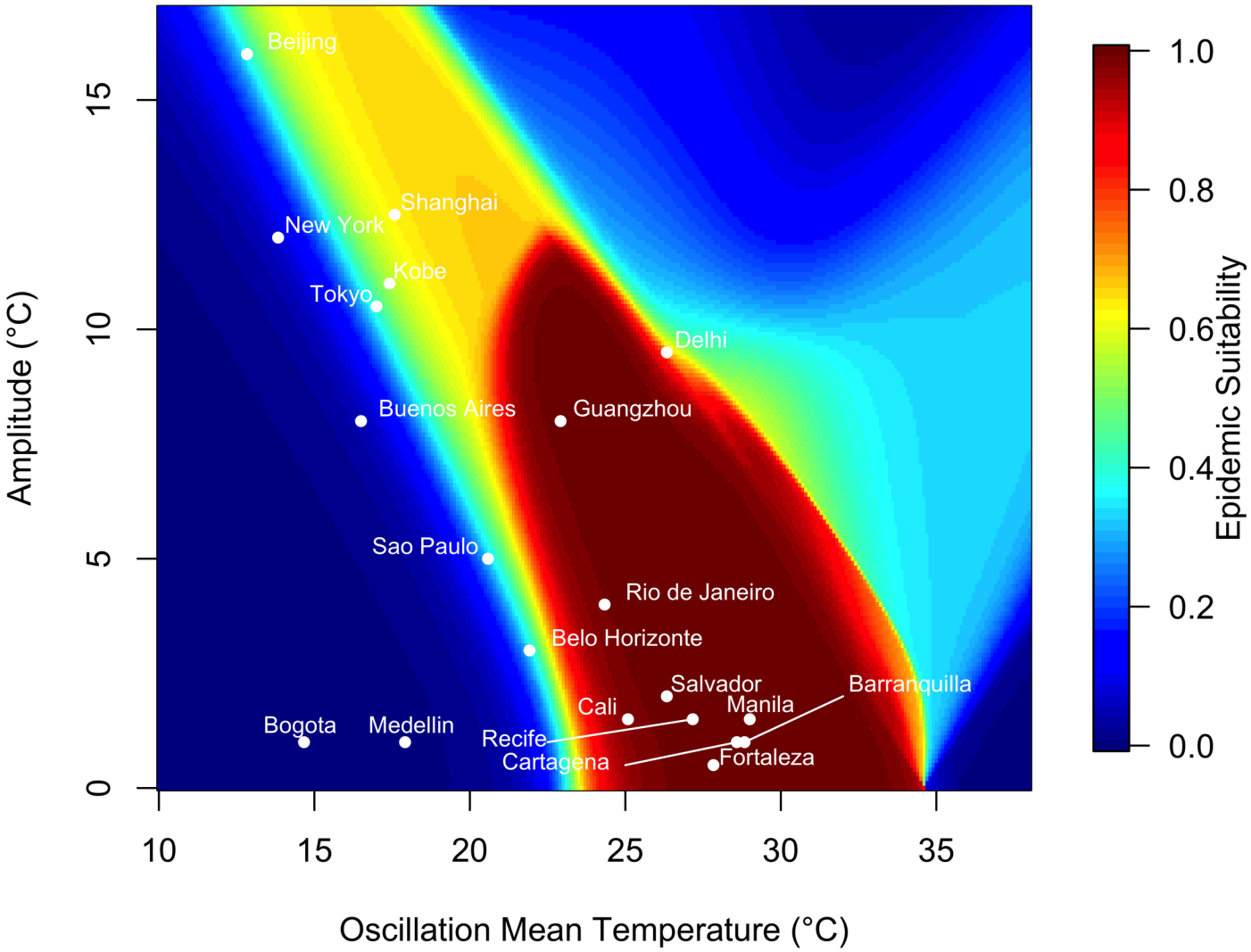

Fig 5. Variation in epidemic suitability across different seasonal temperature regimes averaged across starting temperatures. The heat map shows the epidemic suitability (represented as the proportion of the total human population infected during an epidemic) as a function of mean annual temperature and temperature range averaged across simulations where the initial temperature was set to the seasonal temperature regime's minimum, mean, or maximum temperature. Here, temperature range is defined as the seasonal variation about the annual mean temperature. Twenty large, globally important cities are plotted to illustrate their epidemic suitability.

https://doi.org/10.1371/journal.pntd.0006451.g005

preparation for future outbreaks. As temperatures rise, the global landscape suitable for such outbreaks will expand and shift geographically, potentially placing a larger proportion of the world's population at risk [24,29,31]. Understanding how local temperature regimes govern epidemic dynamics is increasingly important for determining resource allocation and control interventions [41]. While previous work has investigated the effects of temperature on DENV, CHIKV, and/or ZIKV transmission, until now we have lacked comprehensive, mechanistic, and dynamic understanding of the effects of seasonally varying temperature on transmission via its (nonlinear) effects on mosquito and parasite traits [27–34]. With our model, which expands on [24] and [25], we show that seasonal temperature mean and amplitude interact with the temperature at epidemic onset to shape the speed and magnitude of epidemics.

At constant temperature, epidemics varied substantially in the rate at which susceptible individuals were depleted. Epidemics simulated at 25˚C and 30˚C reached similar sizes but the epidemic at 25˚C proceeded at a much slower rate (Fig 2). This "slow burn" phenomenon occurs because slower depletion of susceptible individuals can produce epidemics of similar size to epidemics that infect people very rapidly. This phenomenon also occurs in more realistic, seasonally varying temperature regimes.

The temperature at which an epidemic started affected dynamics only under large ranges of temperature variation. When temperature ranged from 10˚C to 40˚C, the final epidemic size peaked at intermediate starting temperatures (24˚C; Fig 3A). However, in highly suitable seasonal environments, final epidemic size was large regardless of the starting temperature (Fig 3B).

At mean starting temperatures, epidemic suitability was sensitive to the interaction between annual temperature mean and seasonal variation. Under low seasonal temperature variation, a narrow band of annual mean temperatures (approximately 25–35˚C) had the highest epidemic suitability (Figs 4 & S2–S5). Outside this band of temperature regimes, suitability diminishes rapidly. Larger seasonal variation in temperature lowers the range of optimal annual mean temperatures (i.e., suitability is high in cooler places with larger seasonal variation in temperature; Fig 4).

The relationship between epidemic suitability and the seasonal temperature regime also depended on the temperature at the epidemic onset. Three distinct relationships emerged (Figs 5 & S6 and S7). At intermediate annual mean temperatures of ~25–35˚C and low seasonal temperature variation (~0–10˚C), epidemic suitability is insensitive to starting temperature because temperature is suitable for transmission year-round. At lower annual mean temperatures (~10–25˚C) and higher seasonal temperature variation (~10–15˚C), epidemic suitability is highest when epidemics start in moderate to warm seasons, and lower when epidemics start during cooler seasons. Finally, at high annual mean temperatures ($>$ 35˚C) and low seasonal temperature variation (~0–10˚C), epidemic suitability is high only when epidemics start at the coldest period of the year, because otherwise the temperature is too warm for efficient transmission. The interaction between temperature mean, annual variation, and starting point sharply illustrates the unimodal effect of temperature on transmission. Models that do not include unimodal effects of temperature (e.g., those with sinusoidal forcing on a transmission parameter) may fail to capture the limits on transmission in warm environments.

With rising mean annual temperatures and increasing seasonal temperature variation due to climate change, the landscape of epidemic suitability is likely to shift. Importantly, areas with previously low epidemic suitability may have increasing potential for transmission year-round. By contrast, warming temperatures may drive epidemics in cities with high current suitability (e.g., Manila, Philippines, Barranquilla, Colombia, and Fortaleza, Brazil) to shift toward cooler months. Thus, climate change may alter not only epidemic size and duration but also seasonal timing globally, as it interacts with other important drivers like rainfall and human behavior.

It is important to note that model-estimated epidemic suitability should be treated as an upper bound on the potential for large epidemics because within highly suitable climate regimes, epidemics can vary in magnitude due to human population size and movement dynamics [28], effective vector control, and other mitigating factors. Likewise, our estimates are conditioned on *Aedes aegypti* presence and virus introduction to support an outbreak.

Although seasonal temperature dynamics provide insight into vector-borne transmission dynamics, other factors like mosquito abundance, vector control, and rainfall also determine transmission dynamics. Thus, temperature must be considered jointly with these factors. Moreover, accurately describing epidemic dynamics of emerging and established vector-borne pathogens will ultimately require integrating realistic models of environmental suitability, as presented here, with demographic, social, and economic factors that promote or limit disease transmission [42,43]. Conversely, we show that the interaction between temperature and the availability of susceptible hosts alone can drive epidemic burnout even in the absence of other limiting factors like vector control and seasonal precipitation. This suggests that correctly representing the nonlinear relationship between temperature and epidemic dynamics is critical for accurately inferring mechanistic drivers of epidemics and, in turn, predicting the efficacy of control interventions.

Supporting information

S1 Fig. Sensitivity of epidemiological indices as a function of starting temperature to the parameterization of life history traits. The red curve represents the median maximum number of humans in the infected class (I_H) at any given point during the simulation. The blue curve represents the median final (or cumulative) epidemic size (R_H at the final time step). The green curve represents the median length of the epidemic (i.e., the point at which the number of infected individuals was below one). Each shaded area represents the 95% credible interval for the epidemiological indices ran under 50 different parameterizations of the life history traits. Here, simulations were run with the temperature conditions: T_{min} = 10˚C, T_{mean} = 25˚C, and T_{max} = 40˚C (A) and T_{min} = 20˚C, T_{mean} = 25˚C, and T_{max} = 30˚C (B).
(TIF)

S2 Fig. Variation in epidemic suitability across different seasonal temperature regimes with 20% population immunity. The heat map shows the epidemic suitability (represented as the proportion of the total human population infected during an epidemic) as a function of mean annual temperature and temperature range assuming 20% population immunity. Here, temperature range is defined as the seasonal variation about the annual mean temperature. Twenty large, globally important cities are plotted to illustrate their epidemic suitability.
(TIF)

S3 Fig. Variation in epidemic suitability across different seasonal temperature regimes with 40% population immunity. The heat map shows the epidemic suitability (represented as the proportion of the total human population infected during an epidemic) as a function of mean annual temperature and temperature range assuming 40% population immunity. Here, temperature range is defined as the seasonal variation about the annual mean temperature. Twenty large, globally important cities are plotted to illustrate their epidemic suitability.
(TIF)

S4 Fig. Variation in epidemic suitability across different seasonal temperature regimes with 60% population immunity. The heat map shows the epidemic suitability (represented as the proportion of the total human population infected during an epidemic) as a function of mean annual temperature and temperature range assuming 60% population immunity. Here,

temperature range is defined as the seasonal variation about the annual mean temperature. Twenty large, globally important cities are plotted to illustrate their epidemic suitability.
(TIF)

S5 Fig. Variation in epidemic suitability across different seasonal temperature regimes with 80% population immunity. The heat map shows the epidemic suitability (represented as the proportion of the total human population infected during an epidemic) as a function of mean annual temperature and temperature range assuming 80% population immunity. Here, temperature range is defined as the seasonal variation about the annual mean temperature. Twenty large, globally important cities are plotted to illustrate their epidemic suitability.
(TIF)

S6 Fig. Variation in epidemic suitability across different seasonal temperature regimes with minimum starting temperature. The heat map shows the epidemic suitability (represented as the proportion of the total human population infected during an epidemic) as a function of mean annual temperature and temperature range. Here, temperature range is defined as the seasonal variation about the annual mean temperature, and the simulation began at the minimum temperature of the regime. Twenty large, globally important cities are plotted to illustrate their epidemic suitability.
(TIF)

S7 Fig. Variation in epidemic suitability across different seasonal temperature regimes with maximum starting temperature. The heat map shows the epidemic suitability (represented as the proportion of the total human population infected during an epidemic) as a function of mean annual temperature and temperature range. Here, temperature range is defined as the seasonal variation about the annual mean temperature, and the simulation began at the maximum temperature of the regime. Twenty large, globally important cities are plotted to illustrate their epidemic suitability.
(TIF)

S8 Fig. The 2.5% quantile of epidemic suitability to the parameterization of life history traits. Epidemic suitability (represented as the proportion of the total human population infected during an epidemic) as a function of mean annual temperature and the temperature range. Temperature varied according to a seasonal temperature regime, and 50 samples of c, T_{min}, and T_{max} were taken from the joint posterior distribution of each trait thermal response from Mordecai et al. [24].
(TIF)

S9 Fig. The 50% quantile of epidemic suitability to the parameterization of life history traits. Epidemic suitability (represented as the proportion of the total human population infected during an epidemic) as mean annual temperature and the temperature range. Temperature varied according to a seasonal temperature regime, and 50 samples of c, T_{min}, and T_{max} were taken from the joint posterior distribution of each trait thermal response from Mordecai et al. [24].
(TIF)

S10 Fig. The 97.5% quantile of epidemic suitability to the parameterization of life history traits. Epidemic suitability (represented as the proportion of the total human population infected during an epidemic) as mean annual temperature and the temperature range. Temperature varied according to a seasonal temperature regime, and 50 samples of c, T_{min}, and T_{max} were taken from the joint posterior distribution of each trait thermal response from

Mordecai et al. [24].
(TIF)

S1 Appendix. Supplementary methods and references.
(PDF)

Author Contributions

Conceptualization: Erin A. Mordecai.

Data curation: John H. Huber, Erin A. Mordecai.

Formal analysis: John H. Huber, Marissa L. Childs, Jamie M. Caldwell, Erin A. Mordecai.

Funding acquisition: Erin A. Mordecai.

Investigation: John H. Huber.

Methodology: John H. Huber, Marissa L. Childs, Jamie M. Caldwell, Erin A. Mordecai.

Project administration: Erin A. Mordecai.

Software: John H. Huber, Marissa L. Childs, Jamie M. Caldwell.

Supervision: Erin A. Mordecai.

Visualization: John H. Huber.

Writing – original draft: John H. Huber.

Writing – review & editing: John H. Huber, Marissa L. Childs, Jamie M. Caldwell, Erin A. Mordecai.

References

1. Gubler DJ. The global emergence/resurgence of arboviral diseases as public health problems. Arch Med Res. 2002; 33: 330–342. PMID: 12234522
2. Faria NR, Azevedo R do S da S, Kraemer MUG, Souza R, Cunha MS, Hill SC, et al. Zika virus in the Americas: Early epidemiological and genetic findings. Science. 2016; 352: 345–349. https://doi.org/10.1126/science.aaf5036 PMID: 27013429
3. Staples JE, Breiman RF, Powers AM. Chikungunya Fever: An Epidemiological Review of a Re-Emerging Infectious Disease. Clin Infect Dis. 2009; 49: 942–948. https://doi.org/10.1086/605496 PMID: 19663604
4. Special Programme for Research and Training in Tropical Diseases, World Health Organization, editors. Dengue: guidelines for diagnosis, treatment, prevention, and control. New ed. Geneva: TDR: World Health Organization; 2009.
5. Gubler DJ. Dengue/dengue haemorrhagic fever: history and current status. Novartis Found Symp. 2006; 277: 3–16; discussion 16–22, 71–73, 251–253. PMID: 17319151
6. Brady OJ, Gething PW, Bhatt S, Messina JP, Brownstein JS, Hoen AG, et al. Refining the global spatial limits of dengue virus transmission by evidence-based consensus. PLoS Negl Trop Dis. 2012; 6: e1760. https://doi.org/10.1371/journal.pntd.0001760 PMID: 22880140
7. Bhatt S, Gething PW, Brady OJ, Messina JP, Farlow AW, Moyes CL, et al. The global distribution and burden of dengue. Nature. 2013; 496: 504–507. https://doi.org/10.1038/nature12060 PMID: 23563266
8. Khan K, Bogoch I, Brownstein JS, Miniota J, Nicolucci A, Hu W, et al. Assessing the origin of and potential for international spread of chikungunya virus from the Caribbean. PLoS Curr. 2014; 6. https://doi.org/10.1371/currents.outbreaks.2134a0a7bf37fd8d388181539fea2da5 PMID: 24944846
9. Perkins TA, Metcalf CJE, Grenfell BT, Tatem AJ. Estimating drivers of autochthonous transmission of chikungunya virus in its invasion of the americas. PLoS Curr. 2015; 7. https://doi.org/10.1371/currents.outbreaks.a4c7b6ac10e0420b1788c9767946d1fc PMID: 25737803
10. Nsoesie EO, Kraemer MU, Golding N, Pigott DM, Brady OJ, Moyes CL, et al. Global distribution and environmental suitability for chikungunya virus, 1952 to 2015. Euro Surveill Bull Eur Sur Mal Transm

Eur Commun Dis Bull. 2016;21. https://doi.org/10.2807/1560-7917.ES.2016.21.20.30234 PMID: 27239817

11. PAHO. Regional Zika Epidemiological Update (Americas) August 25, 2017. Pan American Health Organization;
12. Bjornstad ON, Finkenstadt BF, Grenfell BT. Dynamics of Measles Epidemics: Estimating Scaling of Transmission Rates Using a Time Series SIR Model. Ecol Monogr. 2002; 72: 169. https://doi.org/10.2307/3100023
13. Coburn BJ, Wagner BG, Blower S. Modeling influenza epidemics and pandemics: insights into the future of swine flu (H1N1). BMC Med. 2009; 7. https://doi.org/10.1186/1741-7015-7-30 PMID: 19545404
14. Kucharski AJ, Funk S, Eggo RM, Mallet H-P, Edmunds WJ, Nilles EJ. Transmission Dynamics of Zika Virus in Island Populations: A Modelling Analysis of the 2013–14 French Polynesia Outbreak. Barker CM, editor. PLoS Negl Trop Dis. 2016; 10: e0004726. https://doi.org/10.1371/journal.pntd.0004726 PMID: 27186984
15. Eisen L, Monaghan AJ, Lozano-Fuentes S, Steinhoff DF, Hayden MH, Bieringer PE. The impact of temperature on the bionomics of Aedes (Stegomyia) aegypti, with special reference to the cool geographic range margins. J Med Entomol. 2014; 51: 496–516. PMID: 24897844
16. Rueda LM, Patel KJ, Axtell RC, Stinner RE. Temperature-dependent development and survival rates of Culex quinquefasciatus and Aedes aegypti (Diptera: Culicidae). J Med Entomol. 1990; 27: 892–898. PMID: 2231624
17. Tun-Lin W, Burkot TR, Kay BH. Effects of temperature and larval diet on development rates and survival of the dengue vector Aedes aegypti in north Queensland, Australia. Med Vet Entomol. 2000; 14: 31–37. PMID: 10759309
18. Kamimura K, Matsuse IT, Takahashi H, Komukai J, Fukuda T, Suzuki K, et al. Effect of temperature on the development of Aedes aegypti and Aedes albopictus. Med Entomol Zool. 2002; 53: 53–58. https://doi.org/10.7601/mez.53.53_1
19. Beserra EB, Fernandes CRM, Silva SA de O, Silva LA da, Santos JW dos. Efeitos da temperatura no ciclo de vida, exigências térmicas e estimativas do número de gerações anuais de Aedes aegypti (Diptera, Culicidae). Iheringia Sér Zool. 2009; 99: 142–148. https://doi.org/10.1590/S0073-47212009000200004
20. Couret J, Dotson E, Benedict MQ. Temperature, larval diet, and density effects on development rate and survival of Aedes aegypti (Diptera: Culicidae). PloS One. 2014; 9: e87468. https://doi.org/10.1371/journal.pone.0087468 PMID: 24498328
21. Watts DM, Burke DS, Harrison BA, Whitmire RE, Nisalak A. Effect of temperature on the vector efficiency of Aedes aegypti for dengue 2 virus. Am J Trop Med Hyg. 1987; 36: 143–152. PMID: 3812879
22. McLean DM, Clarke AM, Coleman JC, Montalbetti CA, Skidmore AG, Walters TE, et al. Vector capability of Aedes aegypti mosquitoes for California encephalitis and dengue viruses at various temperatures. Can J Microbiol. 1974; 20: 255–262. PMID: 4132612
23. Altizer S, Dobson A, Hosseini P, Hudson P, Pascual M, Rohani P. Seasonality and the dynamics of infectious diseases. Ecol Lett. 2006; 9: 467–484. https://doi.org/10.1111/j.1461-0248.2005.00879.x PMID: 16623732
24. Mordecai EA, Cohen JM, Evans MV, Gudapati P, Johnson LR, Lippi CA, et al. Detecting the impact of temperature on transmission of Zika, dengue, and chikungunya using mechanistic models. PLoS Negl Trop Dis. 2017; 11: e0005568. https://doi.org/10.1371/journal.pntd.0005568 PMID: 28448507
25. Yang HM, Macoris MLG, Galvani KC, Andrighetti MTM, Wanderley DMV. Assessing the effects of temperature on dengue transmission. Epidemiol Infect. 2009; 137: 1179–1187. https://doi.org/10.1017/S0950268809002052 PMID: 19192323
26. Yang HM, Boldrini JL, Fassoni AC, Freitas LFS, Gomez MC, de Lima KKB, et al. Fitting the Incidence Data from the City of Campinas, Brazil, Based on Dengue Transmission Modellings Considering Time-Dependent Entomological Parameters. PloS One. 2016; 11: e0152186. https://doi.org/10.1371/journal.pone.0152186 PMID: 27010654
27. Johansson MA, Powers AM, Pesik N, Cohen NJ, Staples JE. Nowcasting the spread of chikungunya virus in the Americas. PloS One. 2014; 9: e104915. https://doi.org/10.1371/journal.pone.0104915 PMID: 25111394
28. Wesolowski A, Qureshi T, Boni MF, Sundsøy PR, Johansson MA, Rasheed SB, et al. Impact of human mobility on the emergence of dengue epidemics in Pakistan. Proc Natl Acad Sci U S A. 2015; 112: 11887–11892. https://doi.org/10.1073/pnas.1504964112 PMID: 26351662
29. Liu-Helmersson J, Stenlund H, Wilder-Smith A, Rocklöv J. Vectorial capacity of Aedes aegypti: effects of temperature and implications for global dengue epidemic potential. PloS One. 2014; 9: e89783. https://doi.org/10.1371/journal.pone.0089783 PMID: 24603439

30. Morin CW, Monaghan AJ, Hayden MH, Barrera R, Ernst K. Meteorologically Driven Simulations of Dengue Epidemics in San Juan, PR. PLoS Negl Trop Dis. 2015; 9: e0004002. https://doi.org/10.1371/journal.pntd.0004002 PMID: 26275146

31. Caminade C, Turner J, Metelmann S, Hesson JC, Blagrove MSC, Solomon T, et al. Global risk model for vector-borne transmission of Zika virus reveals the role of El Niño 2015. Proc Natl Acad Sci U S A. 2017; 114: 119–124. https://doi.org/10.1073/pnas.1614303114 PMID: 27994145

32. Lourenço J, Recker M. The 2012 Madeira dengue outbreak: epidemiological determinants and future epidemic potential. PLoS Negl Trop Dis. 2014; 8: e3083. https://doi.org/10.1371/journal.pntd.0003083 PMID: 25144749

33. Faria NR, da Costa AC, Lourenço J, Loureiro P, Lopes ME, Ribeiro R, et al. Genomic and epidemiological characterisation of a dengue virus outbreak among blood donors in Brazil. Sci Rep. 2017; 7: 15216. https://doi.org/10.1038/s41598-017-15152-8 PMID: 29123142

34. Lourenço J, Maia de Lima M, Faria NR, Walker A, Kraemer MU, Villabona-Arenas CJ, et al. Epidemiological and ecological determinants of Zika virus transmission in an urban setting. eLife. 2017; 6. https://doi.org/10.7554/eLife.29820 PMID: 28887877

35. Duong V, Lambrechts L, Paul RE, Ly S, Lay RS, Long KC, et al. Asymptomatic humans transmit dengue virus to mosquitoes. Proc Natl Acad Sci U S A. 2015; 112: 14688–14693. https://doi.org/10.1073/pnas.1508114112 PMID: 26553981

36. Appassakij H, Khuntikij P, Kemapunmanus M, Wutthanarungsan R, Silpapojakul K. Viremic profiles in asymptomatic and symptomatic chikungunya fever: a blood transfusion threat? Transfusion (Paris). 2013; 53: 2567–2574. https://doi.org/10.1111/j.1537-2995.2012.03960.x PMID: 23176378

37. Murphy BR, Whitehead SS. Immune response to dengue virus and prospects for a vaccine. Annu Rev Immunol. 2011; 29: 587–619. https://doi.org/10.1146/annurev-immunol-031210-101315 PMID: 21219187

38. Weaver SC, Osorio JE, Livengood JA, Chen R, Stinchcomb DT. Chikungunya virus and prospects for a vaccine. Expert Rev Vaccines. 2012; 11: 1087–1101. https://doi.org/10.1586/erv.12.84 PMID: 23151166

39. Le Menach A, McKenzie FE, Flahault A, Smith DL. The unexpected importance of mosquito oviposition behaviour for malaria: non-productive larval habitats can be sources for malaria transmission. Malar J. 2005; 4: 23. https://doi.org/10.1186/1475-2875-4-23 PMID: 15892886

40. Palamara GM, Childs DZ, Clements CF, Petchey OL, Plebani M, Smith MJ. Inferring the temperature dependence of population parameters: the effects of experimental design and inference algorithm. Ecol Evol. 2014; 4: 4736–4750. https://doi.org/10.1002/ece3.1309 PMID: 25558365

41. Perkins TA. Retracing Zika's footsteps across the Americas with computational modeling. Proc Natl Acad Sci U S A. 2017; 114: 5558–5560. https://doi.org/10.1073/pnas.1705969114 PMID: 28533416

42. Zhang Q, Sun K, Chinazzi M, Pastore Y Piontti A, Dean NE, Rojas DP, et al. Spread of Zika virus in the Americas. Proc Natl Acad Sci U S A. 2017; 114: E4334–E4343. https://doi.org/10.1073/pnas.1620161114 PMID: 28442561

43. Alex Perkins T, Siraj AS, Ruktanonchai CW, Kraemer MUG, Tatem AJ. Model-based projections of Zika virus infections in childbearing women in the Americas. Nat Microbiol. 2016; 1: 16126. https://doi.org/10.1038/nmicrobiol.2016.126 PMID: 27562260